inorganics

MDPI

Article

Photoluminescence Properties of X-Ray Generated Divalent Sm in Mechanochemically Prepared Nanocrystalline CaF_2:Sm^{3+}

Z. Siti Rozaila [1], Nicolas Riesen [2] and Hans Riesen [1,*]

[1] School of Science, The University of New South Wales, Canberra, ACT 2600, Australia; sitirozaila91@gmail.com
[2] ARC Research Hub for Integrated Devices for End-User Analysis at Low-Levels (IDEAL), Future Industries Institute, STEM, University of South Australia, Mawson Lakes, SA 5095, Australia; nicolas.riesen@unisa.edu.au
* Correspondence: h.riesen@unsw.edu.au

Abstract: In this study, the mechanochemical preparation of nanocrystalline CaF_2:Sm^{3+} by ball milling calcium acetate hydrate, samarium (III) acetate hydrate, and ammonium fluoride is reported. The photoluminescence of the as-prepared CaF_2:Sm^{3+} shows predominantly Sm^{3+} $^4G_{5/2} \rightarrow {}^6H_J$ (J = 5/2, 7/2, 9/2, and 11/2) f-f luminescence, but intense electric dipole allowed $4f^5$5d (T_{1u}) $\rightarrow$ $4f^6$ $^7F_1$ (T_{1g}) luminescence by Sm^{2+} was generated upon X-irradiation. In comparison with the co-precipitated CaF_2:Sm^{3+}, the conversion of $Sm^{3+} \rightarrow Sm^{2+}$ in the ball-milled sample upon X-irradiation is significantly lower. Importantly, the present results indicate that the crystallite size and X-ray storage phosphor properties of the lanthanide-doped nanocrystalline CaF_2 can be modified by adjusting the ball milling time, dopant concentration and post-annealing treatment, yielding crystallite sizes as low as 6 nm under specific experimental conditions.

Keywords: ball milling; dopant concentration; post-annealing treatment; calcium fluoride; samarium

Citation: Rozaila, Z.S.; Riesen, N.; Riesen, H. Photoluminescence Properties of X-Ray Generated Divalent Sm in Mechanochemically Prepared Nanocrystalline CaF_2:Sm^{3+}. *Inorganics* **2024**, *12*, 332. https://doi.org/10.3390/inorganics12120332

Academic Editor: Binbin Chen

Received: 27 November 2024
Revised: 16 December 2024
Accepted: 17 December 2024
Published: 20 December 2024

1. Introduction

CaF_2 belongs to the alkaline earth metal fluoride (MF_2) compounds which crystallize in the cubic structure with the $Fm\bar{3}m$ space group [1,2]. The Ca^{2+} ions lie at the nodes in the face-centred lattice, while F^- lies at the centre of the octants [3,4]. There has been growing interest in studying the optical properties of lanthanide (Ln)-doped CaF_2 due to its high transmittance properties from the far-UV to the mid-IR range, and the high chemical resistance and low refractive index of this host [5].

Nanocrystalline CaF_2:Ln has been prepared by a wide variety of methods, such as co-precipitation [6–8], the sol–gel process [9], hydrothermal synthesis [10,11], and thermal decomposition of precursors [12]. In recent years, high-energy ball milling has increasingly been applied to synthesize stoichiometric and non-stoichiometric solid solutions with minimal or solvent free routes [13–16]. In this process, the mechanical energy caused by the high speed collision of balls in the ball milling jar forces the reagents to react and turn into fine powders that can be on the nanoscale [17]. This method has advantages of increasing the material reactivity, and uniformity of the spatial distribution of elements, and in reducing the possibility of multi-phase formation [18,19]. Heise et al. successfully synthesized Eu^{3+}-doped MF_2 (M = Ca, Sr, and Ba) powders by ball milling $M(OAc)_2$, $Eu(OAc)_3$ and NH_4F, and crystallite sizes in the range of 12 to 18 nm were obtained [20]. Molaiyan and Witter also reported the preparation of the CaF_2:Sm^{3+} electrolyte by ball milling anhydrous CaF_2 and SmF_3 in stoichiometric compositions of $Sm_{1-y}Ca_yF_{3-y}$ ($0 \leq y \leq 0.15$), using a Tanchen planetary ball mill [15]. Although ball milling is a facile method for preparing nanocrystalline powders, this method has still not been widely applied for the preparation of MF_2:Ln materials for optical applications.

We have previously reported that nanocrystalline CaF_2:Sm^{3+} prepared by a co-precipitation method can serve as a relatively efficient photoluminescent X-ray storage phosphor, with the storage mechanism based on the reduction of Sm^{3+} to Sm^{2+} upon exposure to X-irradiation [21]. It is worth noting that in this case about 65% of trivalent Sm was successfully converted to divalent Sm upon 850 Gy X-irradiation. Samarium-doped systems can be highly sensitive to X-rays, and there is continued interest in identifying potential candidates that display the fast X-ray conversion of Sm^{3+} to Sm^{2+} for applications in dosimetry and computed radiography. In the present study, we report the mechanochemical synthesis of nanocrystalline CaF_2:Sm^{3+} by ball milling $Ca(OAc)_2$, $Sm(OAc)_3$, and NH_4F at room temperature. The synthesized powders were characterized by XRD, electron microscopy, and luminescence spectroscopy. The effects of the ball milling time, Sm concentration, and post-annealing on the generation of Sm^{2+} by X-ray were investigated in detail using photoluminescence measurements.

2. Results and Discussion

The XRD patterns of nanocrystalline CaF_2:0.1%Sm^{3+}, which were prepared by ball milling for periods of 1, 3, 5 and 8 h, are shown in Figure 1a. In Figure 1b, the XRD patterns of CaF_2:$y$$Sm^{3+}$ ball milled for 8 h with different concentrations of Sm^{3+} ($0 \leq y \leq 5\%$) are illustrated. Finally, in Figure 1c, the XRD patterns of CaF_2:0.1%Sm^{3+} (8 h ball milling period) annealed at temperatures of 200, 300, and 400 °C are shown. The patterns were compared with the standard CaF_2 data (PDF-1000043) taken from the Crystallography Open Database [22]. Results from Rietveld refinements obtained by the MAUD 2.93 [23] software package are summarized in Table 1. The goodness of fit $G = R_{wp}/R_{exp}$ is <1.5 for all refinements, i.e., implying good fits [24]. As follows from the figures, all the prominent peaks could be indexed to the cubic CaF_2 structure with the $Fm\bar{3}m$ space group [1,2].

As observed in Figure 1a, impurity peaks are still visible after 1 h of milling. A more complete phase formation of nanocrystalline CaF_2 can be observed after 3 h. Importantly, prolonged ball milling broadened the diffractions peaks, and this was caused by the decrease of the average crystallite size of CaF_2:0.1%Sm^{3+} from 12 ± 1 to 8 ± 1 nm for ball milling times of 1 to 8 h (Table 1a). A 0.14% expansion of the lattice parameter was also observed with this decrease in the crystallite size. It is noted here that the use of hydrated salts in ball milling may accelerate the formation of CaF_2:$y$$Sm^{3+}$ due to the higher mobility of ions and this was also previously observed in the preparation of nanocrystalline BaFCl [25].

Interestingly, a reduction of the average crystallite size of CaF_2:$y$$Sm^{3+}$ from 12 ± 1 to 6 ± 1 nm (Table 1b) was observed when the Sm^{3+} concentration was increased from 0 to 5%. The lattice parameter also increased by 0.17% in this case. The latter is most likely caused by the mechanism of charge compensation as Sm^{3+} substitutes Ca^{2+}. The excess positive charge must be compensated by defects such as O^{2-} impurity ions, substituting F^- in the lattice, and/or interstitial F^-. Also, the electronic repulsion of the ions may increase the lattice parameter [26,27]. Importantly, Sm^{3+} can easily substitute Ca^{2+} in the O_h symmetry with eightfold (bcc) coordination, due to their similar ionic radii (Sm^{3+} = 1.08 Å, compared to Ca^{2+} = 1.12 Å) [28] and, importantly, phase purity is retained for Sm^{3+} concentrations up to 5%.

As follows from Figure 1c, the annealing of CaF_2:0.1% Sm^{3+} at 200, 300, and 400 °C significantly narrowed the diffraction peaks. From the Rietveld refinements, average crystallite sizes of 12, 22, and 46 ± 1 nm were obtained, respectively, for these annealing temperatures (Table 1c). The crystallite size appeared to grow by $\sim T^{3.4}$ upon annealing up to 400 °C. Notably, at the higher annealing temperature of 1100 °C, the crystallographic phase purity of CaF_2:0.1% Sm^{3+} is lost, and multiple additional phases are observed in the XRD pattern.

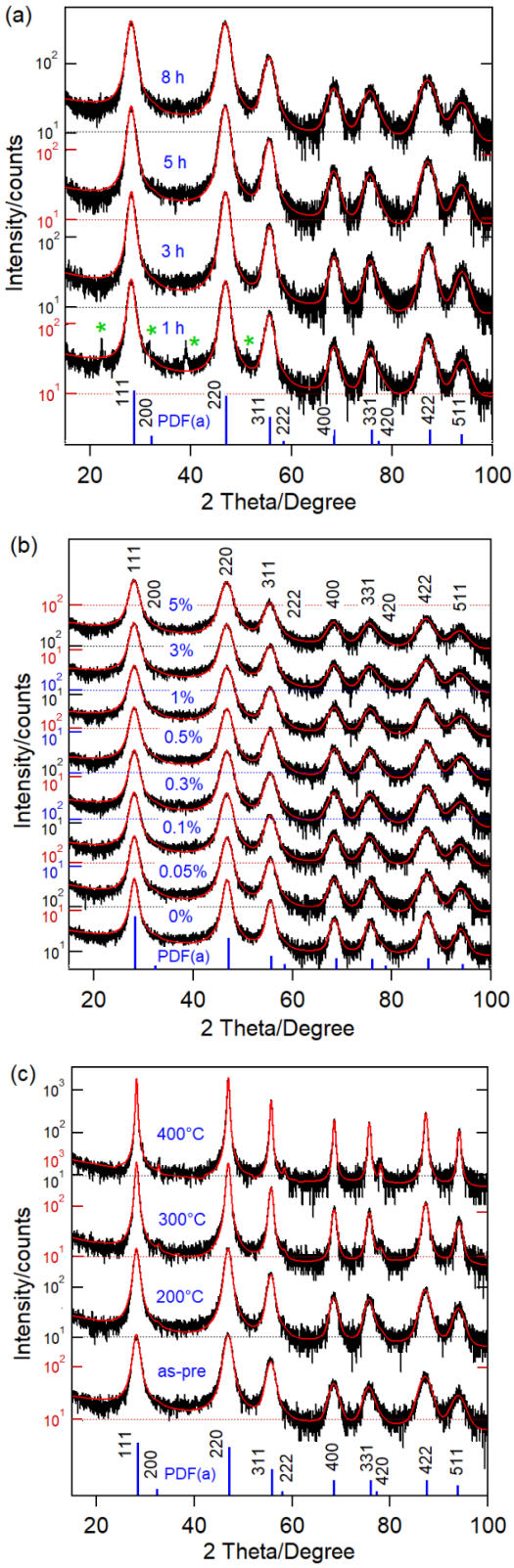

Figure 1. XRD patterns (semi-logarithmic plot) of (**a**) nanocrystalline CaF_2:0.1% Sm^{3+} prepared by ball milling for 1, 3, 5 and 8 h, (**b**) nanocrystalline CaF_2:$y$$Sm^{3+}$ with different concentrations of Sm^{3+} ($0 \leq y \leq 5\%$) ball milled for 8 h, and (**c**) nanocrystalline CaF_2:0.1%Sm^{3+} as prepared by ball milling for 8 h and subsequently annealed at 200, 300, and 400 °C. Experimental data and Rietveld refinements are shown as black and red lines, respectively. The standard data of cubic CaF_2 (PDF-1000043) is shown in blue. The green asterisks indicate impurity phases.

Table 1. Summary of XRD results obtained from Rietveld refinements. R_{wp} and R_{exp} are the weighted-profile *R*-factor and expected *R*-factor. *G* is the goodness of fit (R_{wp}/R_{exp}).

(**a**) Ball milling time CaF_2: 0.1% Sm^{3+}					
Time (h)	Average crystallite size ± 1 (nm)	Lattice parameter, a (Å)	Rietveld refinement		
			R_{wp} %	R_{exp} %	*G*
1	12	5.4754 ± 0.0012	18.9	14.5	1.30
3	11	5.4763 ± 0.0010	19.0	15.1	1.26
5	9	5.4823 ± 0.0012	19.4	14.9	1.30
8	8	5.4832 ± 0.0013	18.5	14.9	1.24
(**b**) Concentration of Sm^{3+} CaF_2: *y*Sm^{3+}, 8 h ball milling time					
y%	Average crystallite size ± 1 (nm)	Lattice parameter, a (Å)	Rietveld refinement		
			R_{wp} %	R_{exp} %	*G*
0	12	5.4824 ± 0.0011	15.9	13.9	1.14
0.05	11	5.4826 ± 0.0012	16.8	13.8	1.22
0.1	9	5.4832 ± 0.0013	18.5	14.9	1.24
0.3	9	5.4838 ± 0.0012	17.4	14.4	1.21
0.5	8	5.4844 ± 0.0011	17.8	15.2	1.17
1	8	5.4864 ± 0.0010	17.3	14.6	1.18
3	7	5.4880 ± 0.0014	17.1	14.5	1.18
5	6	5.4915 ± 0.0017	17.2	14.6	1.18
(**c**) Annealing temperature CaF_2: 0.1% Sm^{3+}, 8 h ball milling time					
Temp. (°C)	Average crystallite size ± 1 (nm)	Lattice parameter, a (Å)	Rietveld refinement		
			R_{wp} %	R_{exp} %	*G*
as-pre	9	5.4774 ± 0.0011	20.9	15.0	1.39
200	12	5.4753 ± 0.0007	19.3	15.4	1.25
300	22	5.4701 ± 0.0004	18.7	15.3	1.22
400	45	5.4687 ± 0.0002	18.7	15.2	1.23

Typical TEM micrographs of CaF_2:0.1%Sm^{3+} prepared by ball milling are displayed in Figure 2. The observed particle size distribution was in qualitative agreement with the average crystallite sizes obtained from the Rietveld refinements. In particular, annealing the sample to 400 °C significantly increased the particle size. A micrograph of CaF_2:0.5%Sm^{3+} prepared by co-precipitation [21] with an average crystallite size of 46 ± 1 nm is shown in Figure 2e for comparison.

Photoluminescence spectra of nanocrystalline CaF_2:0.1%Sm^{3+} prepared by ball milling for 8 h before and after 360 Gy X-irradiation (Cu-Kα) are shown in Figure 3. Sm^{3+} emission lines centred at 566, 604, 645 and 704 nm (Figure 3a) correspond to $^4G_{5/2} \rightarrow {}^6H_J$ (J = 5/2, 7/2, 9/2, and 11/2) f-f transitions, respectively [29–31]. Sm^{3+} $^4G_{5/2} \rightarrow {}^6H_{5/2}$ and $^6H_{7/2}$ transitions contain magnetic and electric dipole contributions that obey the selection rules $\Delta J = 0, \pm 1$, while the other two transitions $^4G_{5/2} \rightarrow {}^6H_{9/2}$ and $^6H_{11/2}$ are purely electric dipole transitions ($\Delta J \leq 6$) [32]. The symmetry of the local environment of the trivalent 4f ions can be identified by the relative intensity ratio of electric dipole to magnetic dipole transitions ($I_R = {}^4G_{5/2} \rightarrow {}^6H_{9/2}/{}^4G_{5/2} \rightarrow {}^6H_{5/2}$) [33]. The present work indicates that most of the Sm^{3+} ions occupied the inversion symmetry sites of the CaF_2 host lattice, since the

IR is <1 [33–35]. Note however that charge compensation will in principle lower the site symmetry.

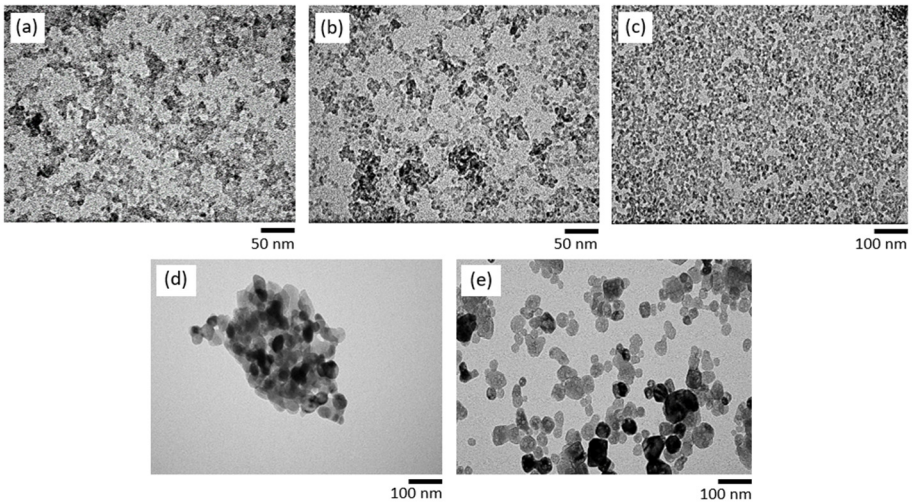

Figure 2. TEM micrographs of nanocrystalline CaF_2:0.1%Sm^{3+}, ball milled for (**a**) 3 h and (**b**) 8 h, annealed at (**c**) 200 °C, (**d**) 400 °C, and (**e**) nanocrystalline CaF_2:0.5%Sm^{3+} prepared by co-precipitation.

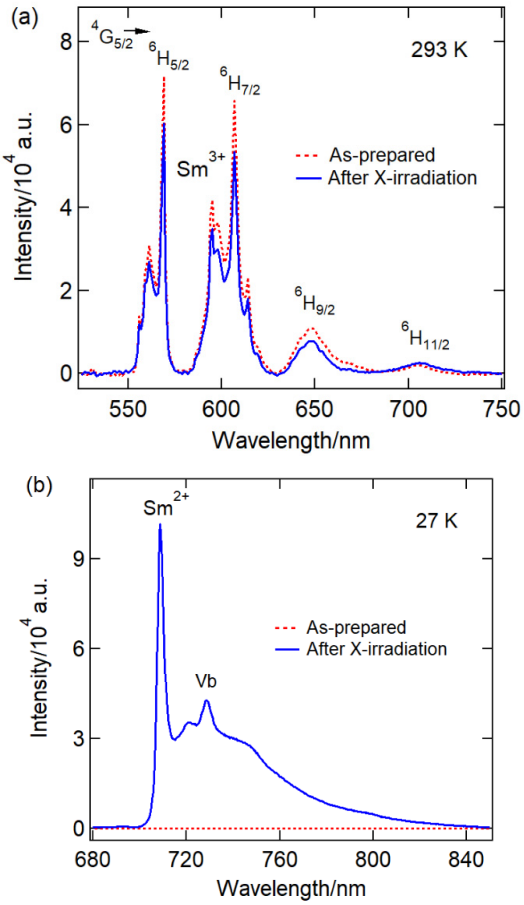

Figure 3. Photoluminescence spectra of nanocrystalline CaF_2:0.1% Sm^{3+} prepared by ball milling for 8 h, before and after 360 Gy X-irradiation. (**a**) Region of Sm^{3+} luminescence at 293 K and (**b**) region of the Sm^{2+} $4f^55d$ (T_{1u}) → $4f^6$ $^7F_1$ (T_{1g}) emission at 27 K.

Upon 360 Gy X-irradiation, the luminescence of Sm^{3+} decreased, as is seen in Figure 3a, accompanied by the rise in the electric dipole allowed Sm^{2+} $4f^55d$ (T_{1u}) → $4f^6$ $^7F_1$ (T_{1g})

transition at 708.2 nm with vibronic side bands (transverse optical phonon mode of CaF_2 due to the O_h^5 group symmetry) (Figure 3b) [36–38]. Note that the Sm^{2+} emission is temperature-dependent and very broad at room temperature [39–41]. We stress here that no Sm^{2+} luminescence was observed before X-irradiation, indicating that the Sm ions entered the CaF_2 host lattice in their +3 oxidation state. In contrast, Liu et al. reported the presence of Sm^{2+} emission lines in the absence of X-irradiation in nanocrystalline BaFCl:Sm^{3+} prepared by ball milling [25].

In Figure 4, the photoluminescence spectra of nanocrystalline CaF_2:0.1%Sm^{3+} are depicted as a function of ball milling time. As follows from Figure 4a, the luminescence of Sm^{3+} increased with a longer milling time. In contrast, the generation of Sm^{2+} upon X-irradiation gradually decreased with increasing ball milling time (Figure 4b). This may be due to better embedding and charge compensation for longer ball milling times, e.g., the closer proximity of the charge compensators to the Sm^{3+} ions. It is also possible that with longer ball milling times, more defects are generated, facilitating efficient non-radiative deactivation paths for the Sm^{2+}.

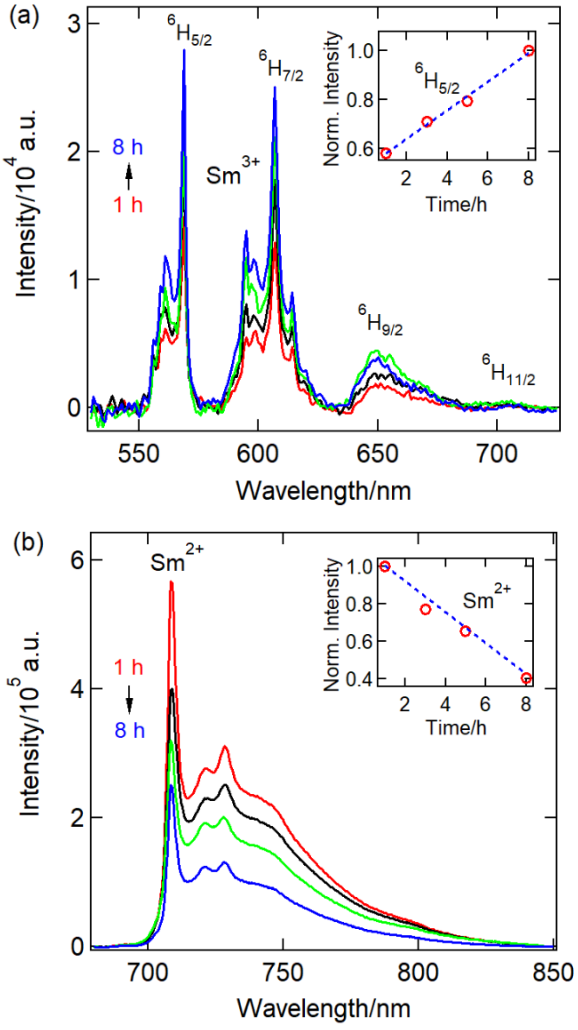

Figure 4. Photoluminescence spectra of nanocrystalline CaF_2:0.1% Sm^{3+} prepared by ball milling for 1, 3, 5, and 8 h (red, black, green and blue traces, respectively). (**a**) Sm^{3+} region at 293 K of the as-prepared sample and (**b**) Sm^{2+} $4f^55d$ (T_{1u}) → $4f^6$ $^7F_1$ (T_{1g}) region at 27 K after 135 Gy X-irradiation. The insets show corresponding integrated intensities (red circles are data points; the blue dotted line is a guide to the eye) as a function of ball milling time.

Photoluminescence spectra of nanocrystalline CaF_2:$y$$Sm^{3+}$ doped with different concentrations of Sm^{3+} ($0.05\% \leq y \leq 5\%$), and ball milled for 8 h are shown in Figure 5. As is

seen in Figure 5a, the intensity of the Sm^{3+} luminescence lines of the as-prepared sample increased with the Sm^{3+} concentration for up to 1%, and then decreased with higher concentrations. Interestingly, the same trend was observed for the Sm^{2+} luminescence (upon 135 Gy X-irradiation) (Figure 5b). This concentration dependence is most likely due to quenching for concentrations higher than 1%, induced by rapid excitation energy transfer between the Sm ions that leads to non-radiative deactivation at trap sites [42].

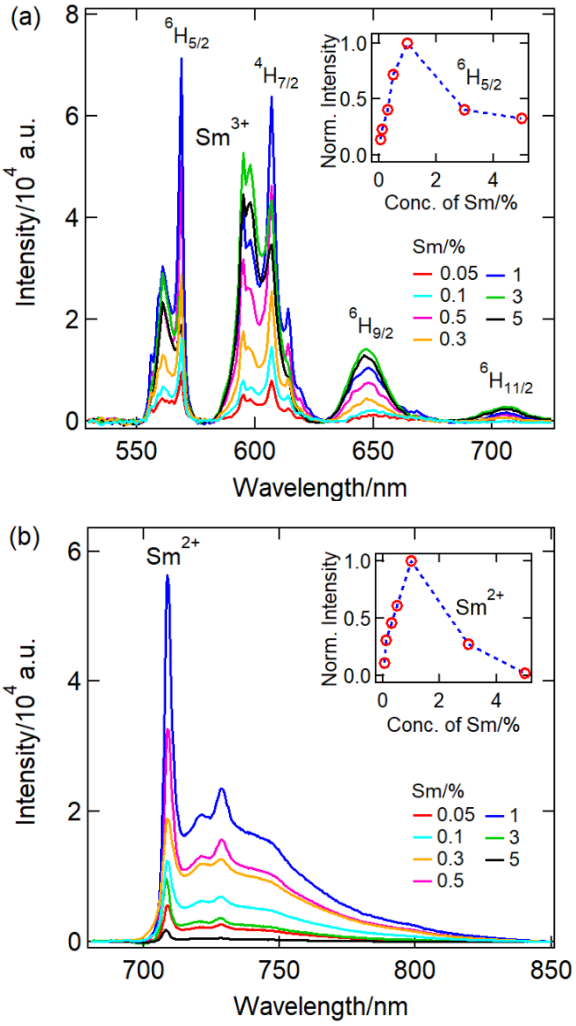

Figure 5. Photoluminescence spectra of CaF_2:ySm^{3+} with $0.05\% \leq y \leq 5\%$ in the region of (**a**) Sm^{3+} at 293 K of the as-prepared sample and (**b**) Sm^{2+} $4f^55d$ (T_{1u}) $\rightarrow$ $4f^6$ $^7F_1$ (T_{1g}) at 27 K upon 135 Gy X-irradiation. Integrated intensities of (**a**) Sm^{3+} $^4G_{5/2} \rightarrow {}^6H_{5/2}$ and (**b**) the Sm^{2+} emission band as a function of Sm concentration are shown in the insets.

In Figure 6, the effect of post-annealing for 1 h at 200, 300, and 400 °C on the luminescence of nanocrystalline CaF_2:0.1%Sm^{3+} (ball milled for 8 h) is summarized. The figure shows that both the Sm^{3+} luminescence of the as-prepared sample (Figure 6a) and the Sm^{2+} luminescence of the X-irradiated samples (Figure 6b) became significantly stronger with increasing annealing temperature. The normalized photoluminescence intensity of the Sm^{3+} and Sm^{2+} emissions followed a $T^{2.4}$ and $T^{2.6}$ power law, respectively. An increase in the photoluminescence intensity of the $Sm^{3+/2+}$ with increased temperature was previously observed by Liu et al. for BaFCl:Sm^{3+} [43].

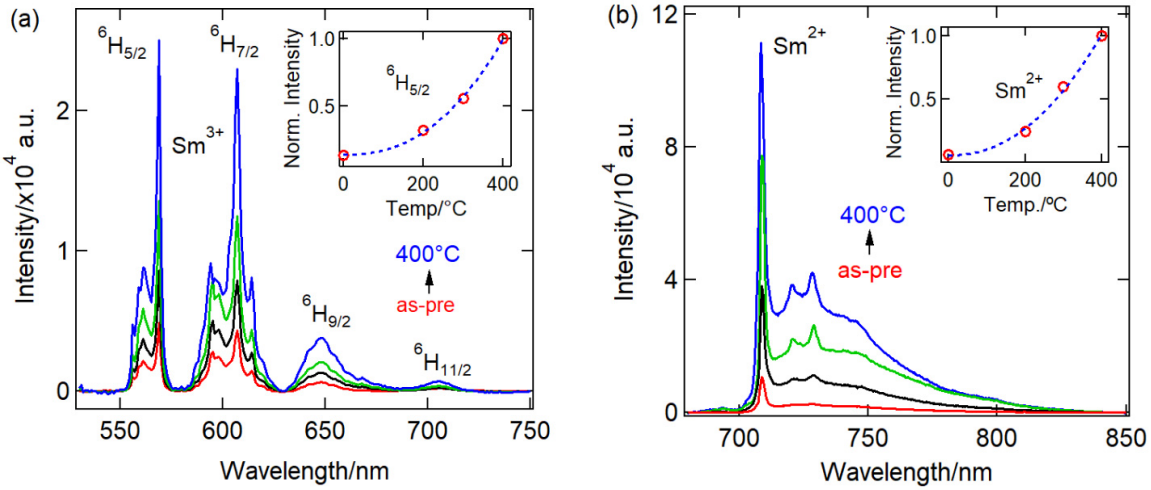

Figure 6. Photoluminescence spectra of CaF_2:0.1%Sm^{3+} annealed at 200, 300, and 400 °C for 1 h in air. (**a**) Sm^{3+} region of the as-prepared sample at 293 K, (**b**) Sm^{2+} region of the 135 Gy X-irradiated sample at 27 K. The insets of (**a**,**b**) show normalized intensities of Sm^{3+} and Sm^{2+} luminescence, respectively (red circles are data points; the blue dotted lines are exponential fits).

In Figure 7 a comparison is shown between the Sm^{2+} luminescence of X-irradiated (100 Gy) nanocrystalline CaF_2:0.5%Sm^{3+} prepared by co-precipitation (CPT), and as-prepared (as well as annealed at 400 °C) CaF_2:0.5%Sm^{3+} prepared by 8 h of ball milling (BM). As seen from the inset of this figure, the Sm^{2+} generation of BM CaF_2:0.5%Sm^{3+} significantly increased by a factor of 23 after annealing at 400 °C, with crystallite size increasing from 8 nm to 44 nm. In addition, both CPT CaF_2:0.5%Sm^{3+} and annealed BM CaF_2:0.5%Sm^{3+} had similar average crystallite sizes of 46 nm and 44 nm, respectively. However, in comparison with the CPT sample, the Sm^{2+} luminescence intensity of the annealed BM sample was lowered by a factor of 3 after 100 Gy X-irradiation. This indicated a faster $Sm^{3+} \rightarrow Sm^{2+}$ conversion upon X-irradiation in the CPT sample when compared to the BM samples. In the BM sample the trivalent Sm^{3+} may be more stabilized by a charge compensator due to the prolonged milling and annealing time, enabling ionic rearrangements of the lattice [44]. However, multiple extra peaks in the Sm^{3+} luminescence were noted in BM CaF_2: 0.5% Sm^{3+} upon annealing at the higher temperature of 1100 °C. This may be related to the extra phases observed in the XRD pattern, which are possibly due to the generation of some oxyfluoride phases.

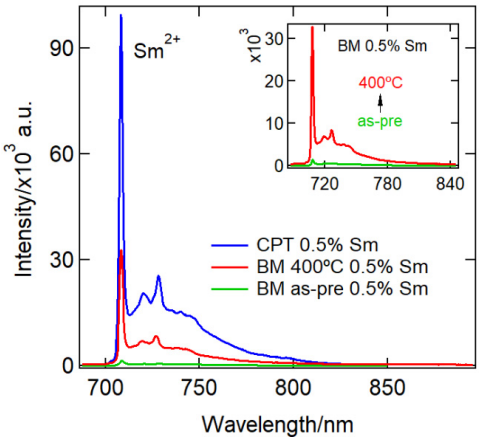

Figure 7. Comparison of photoluminescence spectra of nanocrystalline CaF_2:0.5%Sm^{3+} prepared by co-precipitation (CPT) and as-prepared (as well as annealed at 400 °C) CaF_2:0.5%Sm^{3+} prepared by 8 h of ball milling (BM). The inset shows a 3x magnification of BM CaF_2:0.5%Sm^{3+}.

3. Experimental Methods

Nanocrystalline CaF_2:$y$$Sm^{3+}$ (y = mol%) was prepared by ball milling $Ca(OAc)_2 \cdot H_2O$ (May & Baker Ltd., Essex, England), $Sm(OAc)_3.xH_2O$ (Sigma Aldrich, Australia), and NH_4F (Sigma Aldrich) according to the following solid-state reaction:

$$\begin{array}{c}(1–y)Ca(OAc)_2 \cdot H_2O + (y)Sm(OAc)_3 \cdot xH_2O + (2+y)NH_4F \rightarrow \\ Ca_{1-y}Sm_yF_{2+y} + (2+y)NH_3 + (2+y)HOAc + \ (1–y+xy)H_2O\end{array} \quad (1)$$

Reagents (with y = 0.1%) were premixed and ground using a mortar and pestle before being transferred into a 12 mL zirconia ball mill jar with six 5 mm diameter zirconia balls. The mixtures were then ball milled for 1, 3, 5 or 8 h to investigate the dependence of physical properties on ball milling time. The ball milling was performed using a Planetary Mill (Pulverisette 7 from Fritsch, Germany) at 10 Hz. The mixture obtained was dried overnight in an oven (Labec, Model H323, Marrickville, Australia) at 60 °C. The final product was then ground using a mortar and pestle to yield a homogenous nanocrystalline powder. Nanocrystalline CaF_2:$y$$Sm^{3+}$ powders with different Sm concentrations (y = 0, 0.05, 0.1, 0.3, 0.5, 1, 3, and 5%) were also prepared with a ball milling time of 8 h. Post-annealing by using a muffle furnace (Labec, CEMLS-SD) was undertaken at temperatures of 200, 300, and 400 °C in air.

The phase purity of samples was characterized by powder X-ray diffraction (XRD) on a Rigaku MiniFlex-600 benchtop diffractometer with Cu-Kα radiation (λ = 0.154 nm, 40 kV and 15 mA) with a scanning step and speed of 0.01° and 0.5°/min, respectively. Data was collected in the 2θ range of 10° to 100°. TEM imaging was undertaken by a Tecnai G2 Spirit transmission electron microscope (FEI, Oregon, USA).

Photoluminescence (PL) spectra of Sm^{3+} were measured by using a Horiba Jobin-Yvon Spex FluoroMax-3 fluorometer (controlled by the FluorEssence software) at room temperature with 405 nm excitation. Sm^{2+} luminescence spectra were recorded on a Spex 500 M monochromator (150 grooves/mm grating), equipped with an Andor iDus camera (DV401A-BV Si CCD). A closed-cycle cryostat (CTI-Cryogenics Cryodyne model 22) was used to cool the sample to 27 K. In this case, the samples were excited by a focused 635 nm laser diode. The powders were manually pressed into a counterbore of 5 mm diameter and 0.5 mm depth on an aluminium holder.

The X-ray based reduction of Sm^{3+} to Sm^{2+} was undertaken on the Rigaku Miniflex-600 benchtop powder XRD diffractometer at a 2θ angle of 30° (dose rate ~15 mGy s^{-1}). The X-ray dose was cross-calibrated against a Sirona (Erlangen, Germany) HELIODENT Plus dental X-ray source.

4. Conclusions

We have reported a direct and facile mechanochemical preparation route for nanocrystalline CaF_2:Sm^{3+} by ball milling Ca(OAc), $Sm(OAc)_2$, and NH_4F at room temperature. The photoluminescence spectra of the as-prepared samples display the Sm^{3+} $^4G_J \rightarrow {}^6H_J$ luminescence lines, whereas X-irradiation generates Sm^{2+} with its characteristic luminescence around 708 nm at low temperatures. A ball milling period of 3 to 4 h was found to result in the best single phase, whereas shorter or longer ball milling times resulted in some impurity phases. A longer ball milling period such as 8 h reduced the efficacy of Sm^{2+} generation by X-irradiation. This is likely due to the stabilization of the trivalent state by embedding the charge compensator in the vicinity of the Sm ion, as well as more effective non-radiative deactivation by the introduction of more defects. Maximum luminescence was observed for the sample with a 1 mol% Sm^{3+} concentration, and at a higher concentration quenching was observed. Interestingly, post-annealing substantially increases the X-ray induced Sm^{3+} to Sm^{2+} conversion. It is noted here that attempts to anneal at higher temperatures such as 1100 °C (in air) generated extra phases in the XRD pattern with an associated change in the Sm^{3+} luminescence spectrum. In comparison with the co-precipitation (CPT)-sample, the Sm^{3+} ion in the ball milling sample (BM) is much more stable. The present results

demonstrated that the X-ray storage efficiency of nanocrystalline CaF_2 can be controlled in the preparation process by varying parameters such as ball milling time, annealing temperature and rare earth ion concentration. This study offers valuable insights into the X-ray storage properties of ball-milled CaF_2:Sm^{3+}, particularly the accelerated reduction of Sm ions, with potential applications in areas such as dosimetry and computed radiography.

Author Contributions: Z.S.R.: Sample preparation, investigation, data curation, formal analysis, writing—original draft. N.R.: TEM analysis, writing—review and editing. H.R.: supervision, conceptualization, methodology, writing—review and editing. All authors have read and agreed to the published version of the manuscript.

Funding: UNSW International Postgraduate Award.

Data Availability Statement: The original contributions presented in this study are included in the article. Further inquiries can be directed to the corresponding author(s).

Acknowledgments: We acknowledge the support of The University of New South Wales (UNSW) at the Australian Defence Force Academy for a University International Postgraduate Award. The authors thank Adelaide Microscopy as well as Nobuyuki Kawashima of the Future Industries Institute at the University of South Australia for assistance with TEM imaging.

Conflicts of Interest: The authors declare no competing financial interests or personal relationships that could have been appeared to influence the work reported in this paper.

References

1. Gerward, L.; Olsen, J.S.; Steenstrup, S.; Malinowski, M.; Åsbrink, S.; Waskowska, A. X-ray Diffraction Investigations of CaF_2 at High Pressure. *J. Appl. Crystallogr.* **1992**, *25*, 578–581. [CrossRef]
2. Hazen, R.M.; Finger, L.W. Calcium fluoride as an internal pressure standard in high-pressure cyrstallography. *J. Appl. Crystallogr.* **1981**, *14*, 234–236. [CrossRef]
3. Song, K.S.; Williams, R.T. Alkaline Earth Fluorides. In *Self-Trapped Excitons*; Springer: Berlin/Heidelberg, Germany, 1993; pp. 96–122.
4. Cheetham, A.; Fender, B.; Cooper, M. Defect structure of calcium fluoride containing excess anions I. Bragg scattering. *J. Phys. C Solid State Phys.* **2001**, *4*, 3107. [CrossRef]
5. Ye, W.; Liu, X.; Qiying, H.; Zhou, Z.; Hu, G. Co-precipitation synthesis and self-reduction of CaF_2:Eu^{2+} nanoparticles using different surfactants. *Mater. Res. Bull.* **2016**, *83*, 428–433. [CrossRef]
6. Cantelar, E.; Sanz-García, J.A.; Sanz-Martín, A.; Muñoz Santiuste, J.E.; Cussó, F. Structural, photoluminescent properties and Judd-Ofelt analysis of Eu^{3+}-activated CaF_2 nanocubes. *J. Alloys Compd.* **2020**, *813*, 152194. [CrossRef]
7. Pandurangappa, C.; Lakshminarasappa, B.N. Optical studies of samarium-doped fluoride nanoparticles. *Philos. Mag.* **2011**, *91*, 4486–4494. [CrossRef]
8. Rozaila, Z.S.; Riesen, H. Photoinduced electron transfer in Eu^{2+} and Sm^{3+} co-doped CaF_2 nanocrystals prepared by co-precipitation. *Opt. Mater.* **2024**, *150*, 115225. [CrossRef]
9. Ritter, B.; Krahl, T.; Rurack, K.; Kemnitz, E. Nanoscale CaF_2 doped with Eu^{3+} and Tb^{3+} through fluorolytic sol–gel synthesis. *J. Mater. Chem. C* **2014**, *2*, 8607–8613. [CrossRef]
10. Yuan, G.; Murai, S.; Tamura, S.; Tomita, K.; Tanaka, K. Enhancement of up- and downconversion photoluminescence from Yb^{3+}, Er^{3+} co-doped CaF_2 nanoparticles deposited on two-dimensional plasmonic arrays. In Proceedings of the Proceedings Volume 11194, Plasmonics IV, Hangzhou, China, 20–23 October 2019.
11. Nakhaei, O.; Shahtahmassebi, N.; Mahmood, R. Synthesis and Characterization of CaF_2 NPs with Co-precipitation and Hydrothermal Method. *J. Nanomed. Nanotechnol.* **2011**, *2*, 116.
12. Quan, Z.; Yang, D.; Yang, P.; Zhang, X.; Lian, H.; Liu, X.; Lin, J. Uniform Colloidal Alkaline Earth Metal Fluoride Nanocrystals: Nonhydrolytic Synthesis and Luminescence Properties. *Inorg. Chem.* **2008**, *47*, 9509–9517. [CrossRef] [PubMed]
13. James, S.; Adams, C.; Bolm, C.; Braga, D.; Collier, P.; Friscic, T.; Grepioni, F.; Harris, K.; Hyett, G.; Jones, W.; et al. Mechanochemistry: Opportunities for new and cleaner synthesis. *Chem. Soc. Rev.* **2011**, *41*, 413–447. [CrossRef] [PubMed]
14. Heise, M.; Scholz, G.; Düvel, A.; Heitjans, P.; Kemnitz, E. Mechanochemical synthesis, structure, and properties of solid solutions of alkaline earth metal fluorides: $Ma_{1-x}Mb_xF_2$ (M: Ca, Sr, Ba). *Solid State Sci.* **2016**, *60*, 65–74. [CrossRef]
15. Molaiyan, P.; Witter, R. Mechanochemical synthesis of solid-state electrolyte $Sm_{1-x}CaxF_{3-x}$ for batteries and other electrochemical devices. *Mater. Lett.* **2019**, *244*, 22–26. [CrossRef]
16. Chowdhury, N.; Riesen, N.; Riesen, H. Yb^{3+} and Er^{3+} Codoped $BaLiF_3$ Nanocrystals for X-ray Dosimetry and Imaging by Upconversion Luminescence. *ACS Appl. Nano Mater.* **2021**, *4*, 6659–6667. [CrossRef]
17. Do, J.-L.; Friščić, T. Mechanochemistry: A Force of Synthesis. *ACS Cent. Sci.* **2017**, *3*, 13–19. [CrossRef]

18. Sadykov, V.A.; Mezentseva, N.V.; Bobrova, L.N.; Smorygo, O.L.; Eremeev, N.F.; Fedorova, Y.E.; Bespalko, Y.N.; Skriabin, P.I.; Krasnov, A.V.; Lukashevich, A.I.; et al. Chapter 12—Advanced Materials for Solid Oxide Fuel Cells and Membrane Catalytic Reactors. In *Advanced Nanomaterials for Catalysis and Energy*; Elsevier: Amsterdam, The Netherlands, 2019; pp. 435–514.
19. Düvel, A.; Wilkening, M.; Uecker, R.; Wegner, S.; Sepelak, V.; Heitjans, P. Mechanosynthesized nanocrystalline $BaLiF_3$: The impact of grain boundaries and structural disorder on ionic transport. *Phys. Chem. Chem. Phys.* **2010**, *12*, 11251–11262. [CrossRef] [PubMed]
20. Heise, M.; Scholz, G.; Krahl, T.; Kemnitz, E. Luminescent properties of Eu^{3+} doped CaF_2, SrF_2, BaF_2 and PbF_2 powders prepared by high-energy ball milling. *Solid State Sci.* **2019**, *91*, 113–118. [CrossRef]
21. Rozaila, Z.S.; Riesen, N.; Riesen, H. Luminescence and photoionization of X-ray generated Sm^{2+} in coprecipitated CaF_2 nanocrystals. *Dalton Trans.* **2021**, *50*, 16205–16213. [CrossRef]
22. Crystallography Open Database. Available online: http://www.crystallography.net/cod/index.php (accessed on 1 December 2019).
23. MAUD. Available online: http://maud.radiographema.eu/ (accessed on 2 December 2019).
24. Zhang, J.; Riesen, H. Photostimulated and persistent luminescence of samarium ions in BaFCl. *J. Lumin.* **2019**, *207*, 188–194. [CrossRef]
25. Liu, Z.; Stevens-Kalceff, M.A.; Wang, X.; Riesen, H. Mechanochemical synthesis of nanocrystalline BaFCl:Sm^{3+} storage phosphor by ball milling. *Chem. Phys. Lett.* **2013**, *588*, 193–197. [CrossRef]
26. Bensalah, A.; Mortier, M.; Patriarche, G.; Gredin, P.; Vivien, D. Synthesis and optical characterizations of undoped and rare-earth-doped CaF_2 nanoparticles. *J. Solid State Chem.* **2006**, *179*, 2636–2644. [CrossRef]
27. Zhi, G.; Song, J.; Mei, B.; Weibing, Z. Synthesis and Characterization of Er^{3+} Doped CaF_2 Nanoparticles. *J. Alloys Compd.* **2011**, *509*, 9133–9137. [CrossRef]
28. Shannon, R.D. Revised Effective Ionic Radii and Systematic Studies of Interatomic Distances in Halides and Chalcogenides. *Acta Crystallogr.* **1976**, *32*, 751–767. [CrossRef]
29. Wells, J.-P.R. Laser Spectroscopy of Alkaline Earth Fluoride Crystals Doped with Trivalent Samarium and Europium Ions. Ph.D. Thesis, University of Canterbury, Christchurch, New Zeland, 1996.
30. Mikhail, P.; Ramseyer, K.; Frei, G.; Budde, F.; Hulliger, J. Bleaching of Sm^{2+} during photoluminescence and cathodoluminescence. *Opt. Commun.* **2001**, *188*, 111–117. [CrossRef]
31. Rabbiner, N. Fluorescence of Sm^{3+} in CaF_2. *Phys. Rev.* **1963**, *130*, 502–506. [CrossRef]
32. Bungala, C.J.; Kumar, M.; Gopal, K. Fluorescence properties and energy transfer mechanism of Sm^{3+} ion in lead telluroborate glasses. *Opt. Mater.* **2011**, *33*, 1643–1647.
33. Jamalaiah, B.C.; Rasool, S.N. Fluorescence properties of Sm^{3+} ions in yttrium aluminum borate phosphors for optical applications. *J. Mol. Struct.* **2015**, *1097*, 161–165. [CrossRef]
34. Lakshminarayana, G.; Yang, R.; Mao, M.; Qiu, J.; Kityk, I.V. Photoluminescence of Sm^{3+}, Dy^{3+}, and Tm^{3+}-doped transparent glass ceramics containing CaF_2 nanocrystals. *J. Non-Cryst. Solids* **2009**, *355*, 2668–2673. [CrossRef]
35. Qiao, Y.-P.; Chen, P. Luminescence, energy transfer, and color adjustment of CaO-CaF_2-Al_2O_3-B_2O_3-SiO_2 glass co-doped with CeO_2 and Sm_2O_3. *J. Non-Cryst. Solids* **2021**, *552*, 120461. [CrossRef]
36. Wood, D.L.; Kaiser, W. Absorption and Fluorescence of Sm^{2+} in CaF_2, SrF_2, and BaF_2. *Phys. Rev.* **1962**, *126*, 2079–2088. [CrossRef]
37. Kelly-Gorham, M.R.K.; DeVetter, B.M.; Brauer, C.S.; Cannon, B.D.; Burton, S.D.; Bliss, M.; Johnson, T.J.; Myers, T.L. Complex refractive index measurements for BaF_2 and CaF_2 via single-angle infrared reflectance spectroscopy. *Opt. Mater.* **2017**, *72*, 743–748. [CrossRef]
38. Kaiser, W.; Spitzer, W.G.; Kaiser, R.H.; Howarth, L.E. Infrared properties of CaF_2, SrF_2, and BaF_2. *Phys. Rev.* **1962**, *127*, 1950–1954. [CrossRef]
39. Rozaila, Z.S.; Hutchison, W.; Riesen, H. Persistent Spectral Hole-Burning and Zeeman Effect of X-ray-Induced Sm^{2+} in CaF_2:Sm^{3+} Nanocrystals. *J. Phys. Chem. C* **2023**, *127*, 16950–16959. [CrossRef]
40. Radzhabov, E.A. Spectroscopy of divalent samarium in alkaline-earth fluorides. *Opt. Mater.* **2018**, *85*, 127–132. [CrossRef]
41. Kaiser, W.; Garrett, C.G.B.; Wood, D.L. Fluorescence and Optical Maser Effects in CaF_2:Sm^{++}. *Phys. Rev.* **1961**, *123*, 766–776. [CrossRef]
42. Qiao, Y.-P. Influence of Sm_2O_3 and CaF_2 Concentration on the Enhancement of Luminescence and Red Colour in Borosilicate Glass. *Trans. Indian Ceram. Soc.* **2021**, *80*, 208–215. [CrossRef]
43. Liu, Z.Q.; Stevens-Kalceff, M.A.; Riesen, H. Effects of Postannealing on the Photoluminescence Properties of Coprecipitated Nanocrystalline BaFCl:Sm^{3+}. *J. Phys. Chem. A* **2013**, *117*, 1930–1934. [CrossRef] [PubMed]
44. Stevens-Kalceff, M.A.; Liu, Z.; Riesen, H. Cathodoluminescence Microanalysis of Irradiated Microcrystalline and Nanocrystalline Samarium Doped BaFCl. *Microsc. Microanal.* **2012**, *18*, 1229–1238. [CrossRef]